Article

Phase-locked photon–electron interaction without a laser

Masoud Taleb[1,2], Mario Hentschel [3], Kai Rossnagel [1,2,4], Harald Giessen [3] & Nahid Talebi [1,2] ✉

Ultrafast photon–electron spectroscopy in electron microscopes commonly requires ultrafast laser setups. Photoemission from an engineered electron source is used to generate pulsed electrons, interacting with a sample excited by the laser pulse at a known time delay. Thus, developing an ultrafast electron microscope demands the exploitation of extrinsic laser excitations and complex synchronization schemes. Here we present an inverse approach to introduce internal radiation sources in an electron microscope based on cathodoluminescence spectroscopy. Our compact method is based on a sequential interaction of the electron beam with an electron-driven photon source and the investigated sample. Such a source in an electron microscope generates phase-locked photons that are mutually coherent with the near-field distribution of the swift electron. We confirm the mutual frequency and momentum-dependent correlation of the electron-driven photon source and sample radiation and determine a degree of mutual coherence of up to 27%. With this level of mutual coherence, we were able to perform spectral interferometry with an electron microscope. Our method has the advantage of being simple, compact and operating with continuous electron beams. It will open the door to local photon–electron correlation spectroscopy of quantum materials, single-photon systems and coherent exciton–polaritonic samples with nanometre resolution.

With the advent of ultrafast electron microscopy[1,2], visualizing photoinduced dynamics in materials such as those of magnetic vortices[3] and chemical reactions[4] has become possible at an unprecedented spatial resolution. In particular, the ability to track the ultrafast dynamics of localized and propagating plasmons[5] in nano-optical systems as well as phonon polaritons in quantum materials[6] has recently boosted the application of ultrafast electron microscopy in the form of photon-induced near-field electron microscopy[7]. Moreover, photon-induced near-field electron microscopy has evolved into a unique tool for tailoring the quantum-path interferences in an extremely controllable system of single-electron wavepackets interacting with optical near fields, prepared in either classical or quantum states[8–12]. Combining real-space and reciprocal-space information with

elastic and inelastic processes in diffraction and electron energy-loss spectroscopy, full information about the fundamental aspects of photon–electron interactions is obtained, either in transmission or scanning electron microscopy[13–16].

In a photon-induced near-field electron microscopy setup, pulsed electron beams are commonly generated by virtue of the photoemission process: an ultrafast laser pulse is used to excite the apex of a sharp tip or other forms of cathodes, generating an electron pulse with a specific degree of spatial coherence, which depends on the electron source. A second laser pulse is then used to coherently induce polarization in the sample at a certain delay with respect to the electron pulse. The stimulated interaction of the electron pulse with the laser-induced near-field excitations leads to the predominantly

[1]Institute of Experimental and Applied Physics, Kiel University, Kiel, Germany. [2]Kiel Nano, Surface and Interface Science (KiNSIS), Kiel University, Kiel, Germany. [3]4th Physics Institute and Research Center SCoPE, University of Stuttgart, Stuttgart, Germany. [4]Ruprecht Haensel Laboratory, Deutsches Elektronen-Synchrotron DESY, Hamburg, Germany. ✉e-mail: talebi@physik.uni-kiel.de
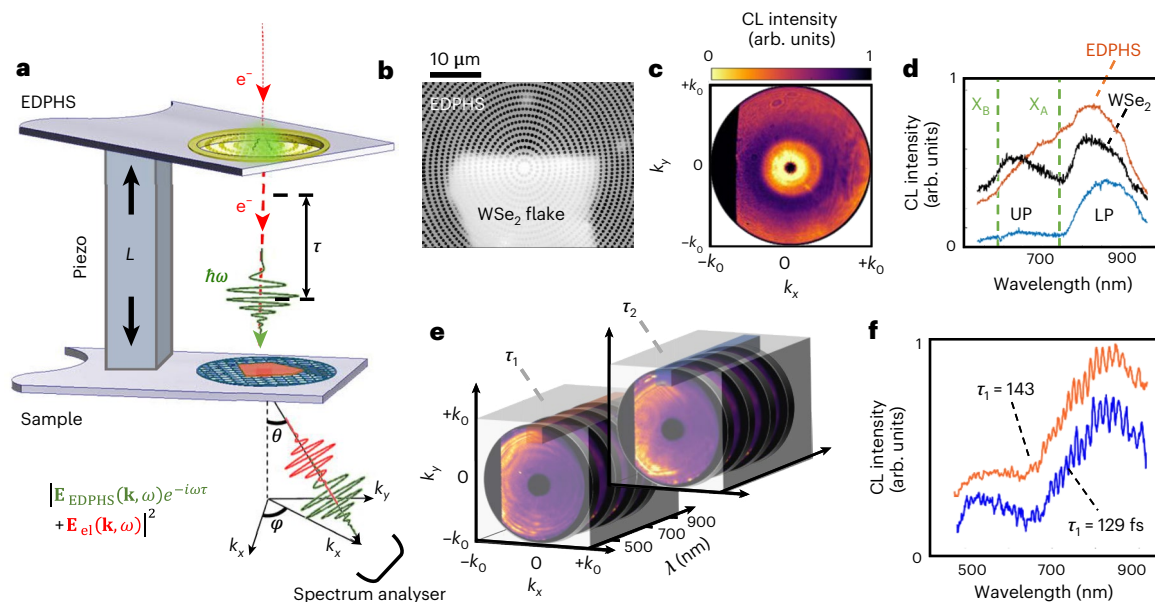
Fig. 1 | Spectral interferometry with an electron beam. a, An electron (e⁻) moving at a kinetic energy of 30 keV interacts with an EDPHS that generates photons with a collimated Gaussian spatial profile. The delay τ between the photon and electron beams arriving at the sample is controlled by distance L between the sample and EDPHS. The energy–momentum distribution of the total scattered field from the sample is detected and analysed to specify the mutual correlation between the EDPHS and sample radiation, as specified in the main text. Due to the excitation of exciton–polaritons with a large lateral wavenumber $k_\parallel$, both EDPHS-induced and electron-induced radiation from the sample are scattered to larger polar angles θ. **b**, SEM image of the combination of EDPHS and sample at a distance of $L = 2\,\mu m$. **c**, Angle-resolved CL pattern of the EDPHS structure. Here, $k_x = k_0\sin\theta\cos\varphi$ and $k_y = k_0\sin\theta\sin\varphi$, where θ and φ are the polar and azimuthal angles with respect to the sample plane. **d**, CL spectra of the EDPHS (red line) and WSe₂ flake (black line), as well as the superposition of both at a distance of $L = 24\,\mu m$ between the EDPHS and sample (blue line), integrated over the entire momentum space. **e**, Schematic of the three-dimensional data cubes (CL intensities versus wavenumbers (k_x, k_y) and wavelength (λ)) at selected delays between the EDPHS and sample. The data shown at the forefront are angle-resolved CL maps of the total field at a filtered wavelength of $800 \pm 10\,nm$. **f**, CL spectra of the total field at $\theta = 45° \pm 2°$ and $\varphi = 100° \pm 2°$. The maps in **e** and **f** are acquired at the indicated delay values of $\tau_1 = 129\,fs$ ($L = 19\,\mu m$) and $\tau_2 = 143\,fs$ ($L = 21\,\mu m$).

longitudinal modulation of the electron beams. The near-field zone of the sample, hence, mediates the transfer of energy and momentum from the coherent laser beam to the sample, where the strength of the photon–electron interactions is controlled by the synchronicity between the near-field excitation and moving electron wavepacket[17–22].

Yet, a visionary application of ultrafast electron microscopy is to coherently control the material's electronic excitations. Due to the high spatial resolution of electron-beam-based characterization techniques, electron beams could be used to coherently drive individual quantum systems to higher states[23] or to probe strong coupling effects[24] or atomic Floquet dynamics[25] in two-level or multilevel quantum systems. Combined with mutually coherent radiation sources, quantum walks on the quantized states of a quantum system, such as quantum dots, defect centres and excitonic systems, could be coherently controlled, by initiating a set of quantum interference paths. Coherent control methods, thus, require a drastic improvement in ultrafast electron microscopy setups to enhance the mutual coherence between photons and electrons such that spectral phases can be retrieved. The latter is crucial, for example, in retrieving quantum interference effects.

To improve the mutual coherence between photon and electron excitations in an electron microscope, we here propose and experimentally realize a proof-of-concept experiment for an inverse approach based on the intrinsic radiation emitted from the electron beam, rather than extrinsic laser radiation, to generate photons that are phase-locked to the near-field distribution of the swift electron. In our setup, an electron beam excites a nanostructured electron-driven photon source (EDPHS)[26–28], which generates well-collimated photon pulses (Fig. 1a,b), as shown by the angle-resolved cathodoluminescence (CL) pattern (Fig. 1c). The EDPHS consists of an array of nanopinholes in a 40 nm gold film deposited on a Si₃N₄ membrane created by

focused-ion-beam milling, with the hole radii gradually varying from 25 nm (holes in the inner rim) to 150 nm (holes in the outer rim). This allows for the generation of broadband photonic radiation (Fig. 1d)[29,30]. The radially propagating surface plasmon polaritons induced by the impacting electrons scatter off the nanopinholes and radiate into the far field in the form of a TM_z-polarized Gaussian wave (Supplementary Note 1 provides a complete characterization of EDPHS radiation).

Due to the difference between the electron group velocity (v) and speed of light in a vacuum (c), the delay between the electrons and photons arriving at the sample can be precisely controlled using a piezo-stage, inserted inside the sample chamber of a scanning electron microscope (SEM). Notably, our setup has six degrees of freedom, allowing to independently move both sample and EDPHS structures by using two nanopositioning stages (Supplementary Note 2 and Supplementary Fig. 2). Specifically, the delay can be described as $\tau = L(v^{-1} - c^{-1})$, where L is the distance between the EDPHS and sample. Given an electron kinetic energy of 30 keV in our experiments ($v = 0.328c$), the delay can be varied in steps of 6.8 as by changing the distance L in steps of 1 nm. Moreover, given the dynamic range of 6 mm for the piezo-stage, the delay can be tuned within the range of 0 fs (corresponding to zero distance or touching point) to 40.8 ps.

For our proof-of-concept experiment, we use thin exfoliated WSe₂ flakes (80 nm thickness) placed on top of a holey carbon transmission electron microscopy grid. Figure 1b shows the SEM image of the WSe₂ flake positioned below the EDPHS, at a distance of $L = 2\,\mu m$ from the EDPHS. Belonging to the class of semiconducting transition metal dichalcogenides, WSe₂ hosts energetically different A and B excitons at room temperature due to spin–orbit coupling, at energies of 1.68 eV ($\lambda = 738$ nm) and 2.05 eV ($\lambda = 604$ nm), respectively. It has previously been demonstrated that excitons can strongly couple to the photonic
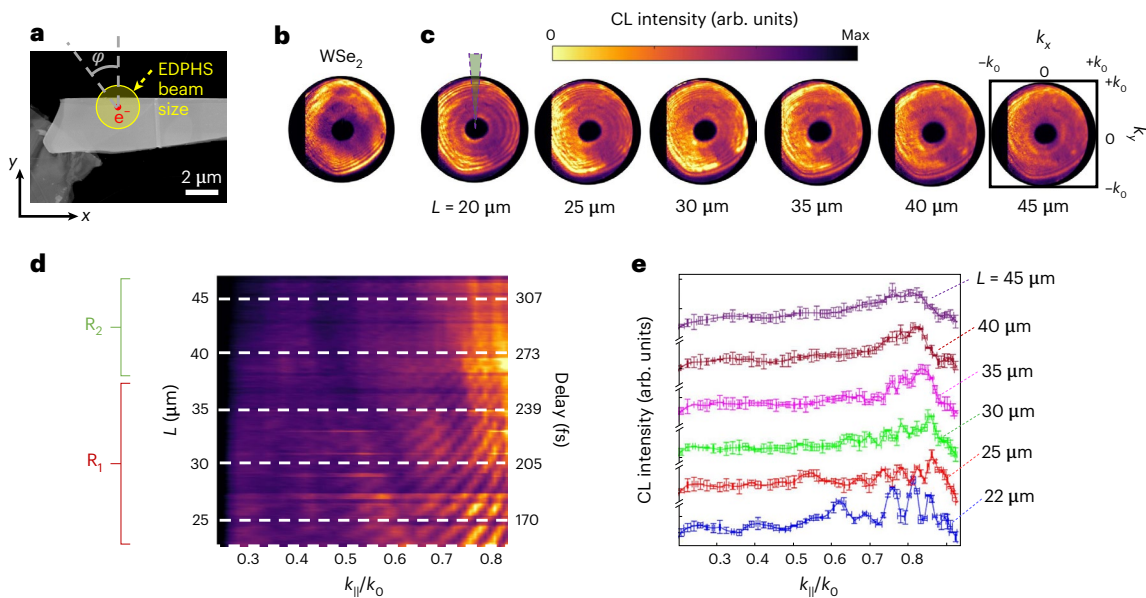
Fig. 2 | Angle-resolved CL maps at the filtered wavelength of λ = 800 nm versus delay τ between the EDPHS and sample. **a**, SEM image of the WSe$_2$ flake. The EDPHS beam size and electron impact position are depicted. **b,c**, Angle-resolved CL maps of the WSe$_2$ flake (**b**) and the combination of WSe$_2$ flake and EDPHS at the indicated distances between them (**c**) ($k_x = k_0 \sin\theta \cos\varphi$ and $k_y = k_0 \sin\theta \sin\varphi$, where θ and φ are the polar and azimuthal angles with respect to the sample plane, respectively). Electrons traverse the flake at a distance of 800 nm from the edge of the flake. **d,e**, Measured L–k CL map acquired at the azimuthal-angle range (marked in **c** with a green triangle) (**d**). Here, $k_{\parallel}^2 = k_x^2 + k_y^2$.

The mutual spatial coherence between the EDPHS and sample radiation is demonstrated by the visibility of interference fringes in region R$_1$. R$_2$ denotes the region in which the visibility of the interference fringes vanishes. All angle-resolved CL maps are taken at a wavelength of 800 nm. The dashed lines in **d** indicate the distances at which the full angle-resolved maps were acquired (as shown in **c**) and at which the the CL intensity–k line plots are shown (**e**). The error bars are depicted on each plot, too. Supplementary Video 1 shows a complete visualization of the interference maps.

modes of thin transition metal dichalcogenide flakes[31,32], where this phenomenon is generally referred to as the self-hybridization effect[32] (Supplementary Fig. 4). This coupling results in an energy splitting and opening of a bandgap, apparent in the dispersion diagram of the guided waves (Supplementary Fig. 5e), as well as the creation of lower-polariton (LP) and upper-polariton (UP) branches that become apparent in the CL spectrum (Fig. 1d)[33,34]. Besides optics-based characterization techniques, electron beams can be used to probe the propagation dynamics and resulting spatial coherence of exciton–polaritons in thin WSe$_2$ flakes using CL spectroscopy[35]. Indeed, electron-beam spectroscopy has been intensively applied to investigate the interaction between excitons and photons or plasmons in hybrid structures[24,36,37]. Here we develop a CL-based technique that allows us to fully determine the amplitude and phase of the aforementioned excitations. More details about the exciton–polaritonic excitations and probing them using CL are provided in Supplementary Note 3.

Using CL, the interference between the transition radiation with the scattering of exciton–polaritons from the edges of the flakes can be used to determine the phase constant of exciton–polaritons, that is, the change in phase per unit length of the propagation of exciton–polaritons. When a moving electron approaches the surface of a flake, an image charge is induced inside the flake that, together with the electron, forms a time-varying dipole. Its annihilation, when the electron crosses the surface, causes ultrabroadband transition radiation. The strong exciton–photon coupling and resulting energy splitting are apparent from the CL spectra of the WSe$_2$ flake (Supplementary Note 3 provides more details about the CL of WSe$_2$ flakes). Thus, the electron beam can excite both LP and UP branches (Fig. 1d, black curve), whereas the EDPHS radiation can most efficiently excite the LP branch, as understood from the spectrum of the EDPHS radiation alone (Fig. 1d, red curve). The overall detected CL signal is the superposition of the electron-beam-induced and EDPHS-induced

scattered field from the sample (Fig. 1a (bottom) and Fig. 1d (blue curve)). Importantly, this spectrum is not a simple direct incoherent superposition of EDPHS and sample radiation. To highlight the interference effects, however, analysing the data within the entire energy–momentum space is required. The degree of mutual coherence between the elements of this superposition is inferred from the results of an interferometry technique outlined here, and discussed step by step below.

The total momentum-resolved CL spectrum is thus rewritten as[38]:

$$\Gamma_{CL}(k_{\parallel}, \omega) = (4\pi\hbar k_0)^{-1} \left\{ |E_{EDPHS}(k_{\parallel}, \omega)|^2 + |E_{el}(k_{\parallel}, \omega)|^2 \right.$$
$$\left. + E_{el}(k_{\parallel}, \omega) \cdot E^*_{EDPHS}(k_{\parallel}, \omega)\, e^{i\omega\tau} + E^*_{el}(k_{\parallel}, \omega) \cdot E_{EDPHS}(k_{\parallel}, \omega)\, e^{-i\omega\tau} \right\},$$
$$(1)$$

where $\hbar$ is the reduced Planck constant; $k_0 = \omega/c$ is the free-space wavenumber of light; $k_{\parallel} = k_0 \sin\theta = (k_x^2 + k_y^2)^{1/2}$ is the parallel wavenumber; and $E_{el}(k_{\parallel}, \omega)$ and $E_{EDPHS}(k_{\parallel}, \omega)$ are the electron-induced and EDPHS-induced electric-field components detected in the far field, respectively. The delay τ is controlled by the distance L between the EDPHS and sample. Hence, by changing the distance between the EDPHS and sample, the observed interference fringes in both frequency and momentum space can be controlled. The visibility of the interference fringes allows for the determination of the degree of mutual coherence between the EDPHS-induced and electron-induced radiation. In addition, spectral interferometry is widely used to characterize the broadening of ultrafast laser pulses. Due to collimated laser pulses, which constitute a paraxial propagation configuration, one can only measure the spectra along the longitudinal direction ($\theta = 0$)[39]. Although the EDPHS radiation itself is collimated, scattering from the WSe$_2$ flake is also observed at larger polar angles. In addition, coherent electron-induced radiation pattern from the flake is a dipolar one[40]
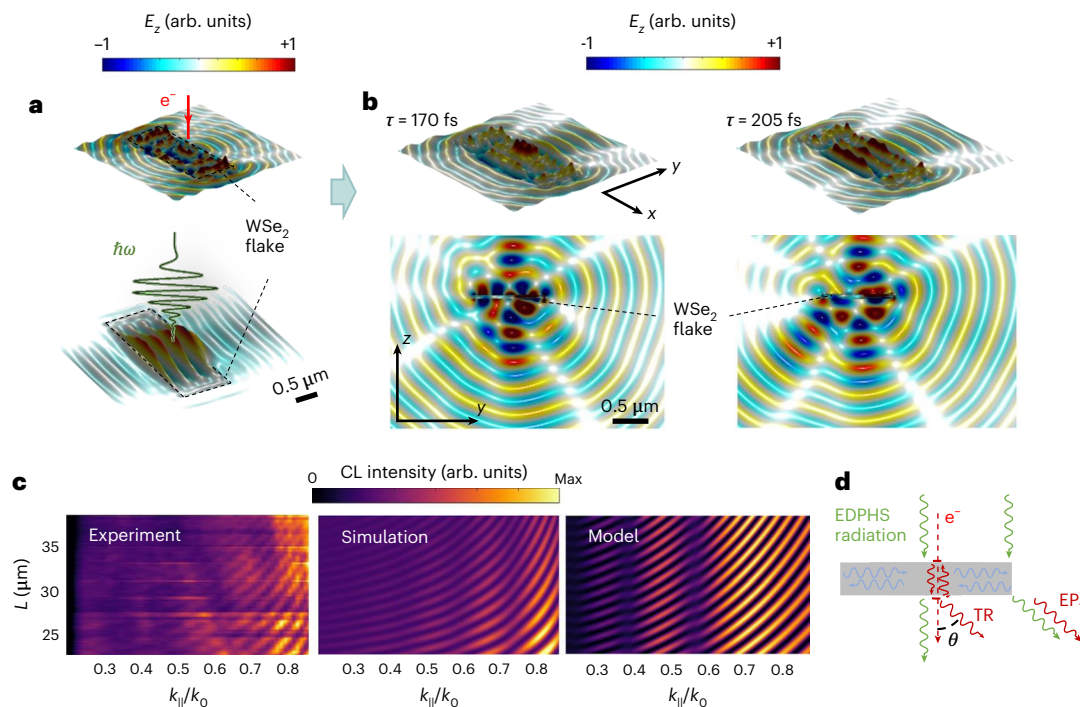
Fig. 3 | Modelling the experimentally observed *k*-space interference fringes. **a,b**, Simulated near-field distributions induced by a moving electron at a kinetic energy of 30 keV (top) and EDPHS radiation (bottom) (**a**) and their superposition at two depicted delay times between the EDPHS radiation and incoming electron beam (**b**) at the *x*–*y* plane located 5 nm above the sample (top row) and the *y*–*z* cross-section cutting parallel to the electron-beam trajectory at the electron-beam impact position (bottom row). **c,d**, Experimental results (left) compared with the simulated CL intensity versus the momentum–distance space (middle) (distance between EDPHS and sample, *L*, as well as the transverse momentum parallel to the shorter symmetry axis of the flake), compared with the analytical results (right) (**c**) obtained using the proposed model (**d**) that considers the interference between a direct transmission of the EDPHS radiation through the film and its scattering from the edge, transition radiation (TR) and scattering of the excited exciton–polaritons (EPs) from the edges. The contributions of EDPHS-induced and electron-induced radiation are shown by the green and red wavy arrows, respectively.

such that angle-resolved spectroscopy is required to fully capture the mutual coherence between EDPHS and sample radiation. Hence, the interference patterns in both momentum and energy space are characterized, and a three-dimensional energy–momentum data cube is acquired, in dependence of delay τ between the EDPHS and sample radiation. For example, by spectrally filtering the total radiation at $\lambda = 800 \pm 10$ nm, the interference maps in the momentum space were observed and analysed (Fig. 1e). Similarly, by filtering the angular distribution of the detected CL signal around $\theta = 45° \pm 2°$ and $\varphi = 100° \pm 2°$, corresponding to $k_{\parallel} = 0.707k_0$ and the azimuthal direction normal to the edge of the flake, the spectral interference fringes can be examined (Fig. 1f). In particular, we notice that when the WSe$_2$ flake is excited with both electron beam and EDPHS radiation, the overall CL spectrum differs from an incoherent superposition of EDPHS and sample CL spectra. More importantly, the total CL angle-resolved maps and spectra vary with distance *L* between the EDPHS and sample (Fig. 1e,f), and delay-dependent *k* space or spectral interferences are observed. Noteworthily, such interference patterns are only observed when EDPHS radiation as well as electron-induced polarization inside the sample show coherent radiation properties. Therefore, polariton excitations such as plasmon polaritons in the EDPHS and exciton–polaritons of the sample could be used for examining the functionality of our approach.

Since the photon generation process relies on the electron-induced surface plasmon polaritons inside the EDPHS, we anticipate that EDPHS radiation has a high degree of mutual coherence with respect to the evanescent field accompanying the electron. Direct proof of this hypothesis is performed by using the subsequent interactions of the electron beam with two similar EDPHS structures (Supplementary Note 1).

To explore the mutual coherence of the EDPHS and sample radiation, we analyse the dependence of the angle-resolved CL patterns on *L*, by choosing a WSe$_2$ flake as the sample (Fig. 2a). The electron-induced radiation of the sample that we generally refer to as sample radiation constitutes the excitation of exciton–polaritons and transition radiation. The mutual correlation function between EDPHS and sample radiation is a function of both wavelength and momentum, as stated above. First, we analyse the correlation between the EDPHS and sample radiation by filtering the overall radiation at the carrier wavelength of EDPHS radiation (that is, $\lambda = 800$ nm) and analysing the angle-resolved radiation pattern. When only the electron beam excites the sample, specific interference fringes in the angle-resolved CL pattern are observed, due to interference between the transition radiation and exciton–polaritons (Fig. 2b and Supplementary Note 3). A drastic alteration in the interference fringes is observed when EDPHS radiation and electron beam simultaneously excite the sample. The momentum–distance interference fringes are observed within the distance range of $L = 22$–40 μm (Fig. 2c,d, region R$_1$) and these interference fringes are altered by including the EDPHS radiation, which is determined by the temporal coherence of the generated EDPHS radiation and decoherence phenomena, due to the interaction of the superimposed EDPHS and sample radiation with the environment. This latter effect is precisely the reason why the visibility of the interference fringes is diminished by further increasing the distance *L* above 40 μm. Performing the measurements in finer steps, we are able to resolve the interference fringes versus the transverse angular momentum and distance *L*, demonstrating the high degree of mutual coherence between EDPHS and sample radiation. The interference fringes—within the fully coherent range—can be simulated using
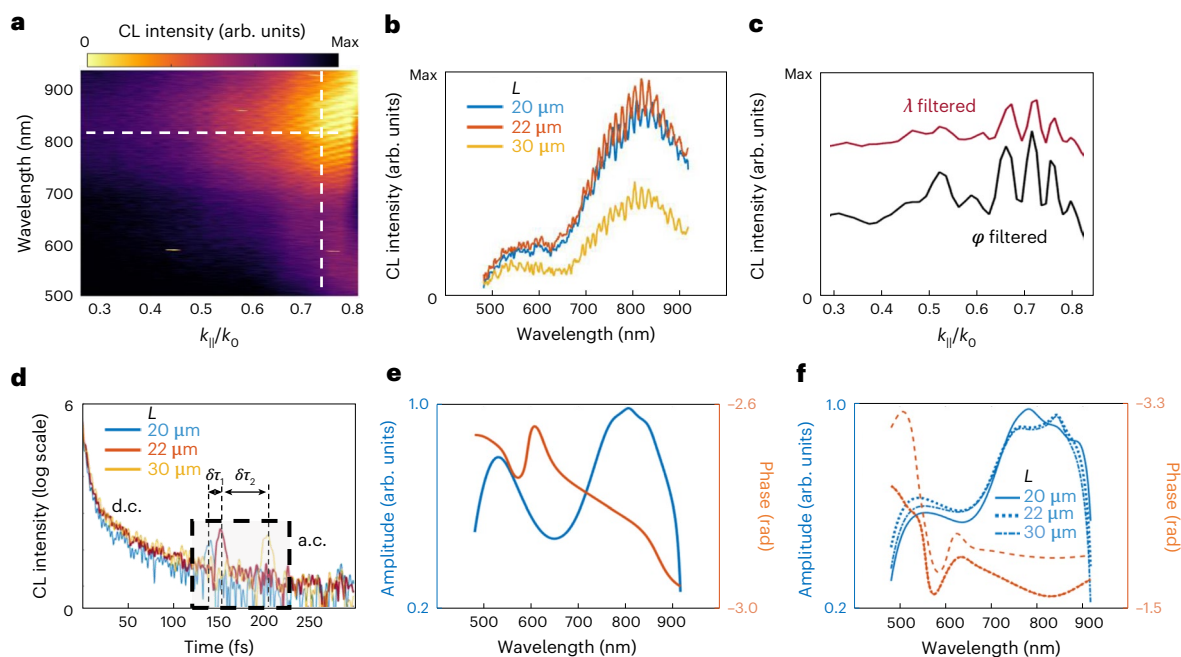
Fig. 4 | Spectral interference fringes. a, Momentum-resolved CL spectra at a distance of $L = 22$ μm (delay $\tau = 150$ fs), for an electron traversing the WSe$_2$ flake at a distance of 2 μm from the edge. **b**, CL intensity acquired at the wavenumber of $k_\parallel = 0.77k_0$ at the depicted distances. **c**, CL intensity versus lateral momentum, where the results obtained by filtering along the azimuthal direction via a mechanical slit and then selecting the spectral content at $\lambda = 800$ nm, are compared with the results obtained by spectrally filtering the radiation at $\lambda = 800$ nm, and then selecting the azimuthal range as $\varphi = 90° \pm 2$. **d**, Fourier-transformed CL intensity at the depicted L values, with three peaks at $t = 0$ (d.c. term) and $t = \pm\tau$ at the depicted distances between the sample and EDPHS. Here $\delta\tau_1 = 14$ fs and $\delta\tau_2 = 55$ fs correspond to $\delta L = 2$ μm and $\delta L = 8$ μm, respectively. **e,f**, Retrieved relative electric-field amplitude and phase with respect to the EDPHS for $k_\parallel = 0.77k_0$ (**e**) using the CL signal acquired for $L = 22$ μm and $k_\parallel = 0.70k_0$ (**f**) using the CL signal acquired for different L values.

classical electromagnetism considering a realistic system of EDPHS and sample radiation (Fig. 3) (Supplementary Notes 3 and 4 provide details of the simulation method). In the simulation, a rectangular WSe$_2$ flake is considered that is sequentially excited by a swift electron at the kinetic energy of 30 keV and EDPHS radiation (the previously performed simulation results, which includes the interaction of the electron beam with our EDPHS structure, is used (Supplementary Fig. 1)). The EDPHS-induced and electron-induced polarizations are superimposed at the corresponding delays (Fig. 3a,b) and the far-field radiation is obtained by projecting the field distributions from the near field to far field, using free-space Green's functions. The delay between the electron-induced and EDPHS-induced polarization affects the total diffraction angle of the field. Instead of the superposition of two waves with the same propagation direction (as for the combination of two identical EDPHS structures (Supplementary Fig. 5)), a directional beam and dipolar-field profile are superimposed. The latter radiation is caused by the transition radiation mechanism as an example. Thus, the interference patterns are highly momentum dependent. The agreement between the simulation and experimental results suggests that the superposition of EDPHS-induced and electron-induced scattered fields from the sample underpin the experimentally observed interference patterns.

To better understand this effect, we propose a model to reconstruct the interference patterns considering different optical pathways in the relaxation and scattering processes of both EDPHS-induced and electron-induced polarizations inside the sample. (Fig. 3d). For this, we consider the possible beam paths that contribute to the far-field patterns as (1) the EDPHS radiation that is directly transmitted through the film, (2) the EDPHS radiation that is scattered off the edge of the flake, (3) the transition radiation and (4) the excitation of the exciton–polaritons and their scattering from the edges. First, we notice that EDPHS excitation cannot directly excite the exciton–polaritons, due

to momentum mismatch between the exciton–polariton dispersion and that of free-space light. The scattering of EDPHS radiation from the edges results in the excitation of exciton–polaritons and forms a standing-wave pattern inside the film that also contributes to the scattered light from the edges (Fig. 3a shows a visualization of the standing-wave pattern and its scattering from the edges). In addition, the electron beam directly excites the exciton–polaritons as well as causes transition radiation (Supplementary Note 3). The interferences between these four beam paths form the interference pattern (Fig. 3d), matching the simulated and experimental results. Minor disagreements are due to the fact that in the model, only scattering from two edges are included, whereas the experimental and simulation results include more scattering edges.

The model, thus, reproduces the measured pattern, further confirming the high degree of mutual coherence between the EDPHS and sample radiation. Comparing the experimental results with the results of classical electromagnetic simulations, a degree of coherence of 27% is inferred. The degree of mutual coherence in this system is affected by the generation of incoherent CL excitation in both EDPHS and sample, due to the generation of randomly distributed electron–hole pairs and incoherent phonon relaxation pathways. Thus, (1) including only aloof electron trajectories for exciting the EDPHS structure, for example, by considering a hole in the middle of the EDPHS structure to avoid the penetration of the electron beams inside the material; (2) cooling the system with cryogenic stages; and (3) using collimated electron beams or beams with a low divergence angle could substantially enhance the degree of mutual coherence.

Increasing the spatial distance to $L > 40$ μm leads to the deterioration of the visibility of interference fringes (Fig. 2d, region R$_2$). This behaviour is a peculiar example of the decoherence phenomena, where the interaction of the individual components of the radiation field with the environment suppresses the mutual coherence of EDPHS-induced

and electron-induced polarization in the sample (Supplementary Note 4 and Supplementary Fig. 6).

The high degree of coherence between the EDPHS and sample radiation, within the aforementioned distance range, is also spectrally analysed and used for spectral interferometry, as demonstrated below. The angle-resolved (momentum-resolved) CL spectra of the combined EDPHS and sample radiation shows a clear interference map at higher-momentum ranges between $k_\parallel = 0.7k_0$ and $k_\parallel = 0.8k_0$ (Fig. 4a). The LP branch is prominently excited, as the EDPHS radiation peaks at 800 nm. Moreover, by changing the delay (distance between the EDPHS and sample), both modulation frequency and visibility of interferences fringes are altered (Fig. 4b). The dependency of the CL signal on $k_\parallel$, using the technique compared here, that is, filtering the signal along the azimuthal degree of freedom using a mechanical slit, is compared with the signal obtained beforehand, where the angle-resolved patterns were obtained at the filtered wavelength of $\lambda = 800$ nm (Fig. 4c). Obviously, good agreement is obtained. These spectral interference fringes are, thus, used to retrieve the spectral phase in the following.

To proceed, we first rewrite equation (1) into three components as[41]:

$$\Gamma_{CL}(\omega) = |I_0(\omega)| \left\{ 1 + |\sigma(\omega)|^2 + \sigma(\omega) e^{i\omega\tau} + \sigma^*(\omega) e^{-i\omega\tau} \right\} \quad (2)$$

at a fixed $k_\parallel$ value, where $\sigma(\omega) = E_{z,el}(\omega)/E_{z,EDPHS}(\omega)$ is the ratio of the z components of the electric field radiated to the far field of the EDPHS and sample, respectively, and $|I_0(\omega)| = (4\pi\hbar k_0)^{-1} |E_{EDPHS}(\omega)|^2$. The first term, that is, $\Gamma_0(\omega) = |I_0(\omega)|\{1 + |\sigma(\omega)|^2\}$, does not have any dependence on delay τ, whereas the last two terms, defined as $\Gamma_+(\omega) = |I_0(\omega)|\sigma(\omega)e^{+i\omega\tau}$ and $\Gamma_-(\omega) = |I_0(\omega)|\sigma^*(\omega)e^{-i\omega\tau}$, clearly depend on the delay. Thus, taking the Fourier transform of the overall CL spectrum, one can transfer all the components into the time domain, with $\tilde{\Gamma}_0(t) = \Im\{\Gamma_0(\omega)\}$ and $\tilde{\Gamma}_\pm(t) = \Im\{\Gamma_\pm(\omega)\}$ centred at $t = 0$, and $t = \pm\tau$, respectively. Now, we perform this for the CL signal at distances of $L = 20$, $L = 22$ and $L = 30$ μm at $k_\parallel = 0.77k_0$, where the time-dependent CL signal is obtained. Three dominant peaks are observed as expected, namely, the d.c. term at $t = 0$, and the a.c. terms at $t = \pm136$ fs for $L = 20$ μm, $t = \pm150$ fs for $L = 22$ μm and $t = \pm204$ fs for $L = 30$ μm. The occurrence of the d.c. term is clearly due to the delay-independent CL intensities corresponding to the individual EDPHS and sample CL signals ($\tilde{\Gamma}_0(t)$; the first two terms on the right-hand side of equation (1)). In addition, the a.c. terms that occur exactly at $\tau = L(v^{-1} - c^{-1})$ are due to the last terms on the right-hand side of equation (1). Assuming that the CL intensities from the EDPHS and sample are at the same level of strength, the degree of mutual coherence is obtained as $CL^{a.c.}/CL^{d.c.}$, which corresponds to exactly 27%, as inferred from the comparison of the simulated and measured results before. The ratio of CL intensities of the EDPHS and sample is experimentally confirmed by taking the CL spectra of the individual components under the same experimental conditions (Fig. 1d). The broadening of the d.c. signal is also acquired by taking the bandwidth of the d.c. peak, which corresponds to a full-width at half-maximum of 5.2 fs. Thus, the temporal broadening of the EDPHS and sample radiation are both approximately 5.2 fs. Taking the inverse Fourier transform of only the a.c. signal and by filtering the time-dependent signal around the a.c. peak, both spectral amplitude and phase are retrieved (Fig. 4c). For doing this, we note that

$$|\Gamma_0(\omega)| / |\Gamma_\pm(\omega)| = \left(1 + |\sigma(\omega)|^2\right) / |\sigma(\omega)|, \quad (3)$$

allowing us to compute the relative electric-field amplitude as

$$|\sigma(\omega)| = \frac{|\Gamma_0(\omega)|}{2|\Gamma_+(\omega)|} - \sqrt{\left(\frac{|\Gamma_0(\omega)|}{2|\Gamma_+(\omega)|}\right)^2 - 1}. \quad (4)$$

Moreover, the relative phase is obtained by simply retrieving the phase of $\Gamma_+(\omega)$, as $|I_0(\omega)|$ is a real-valued quantity. Moreover, since the
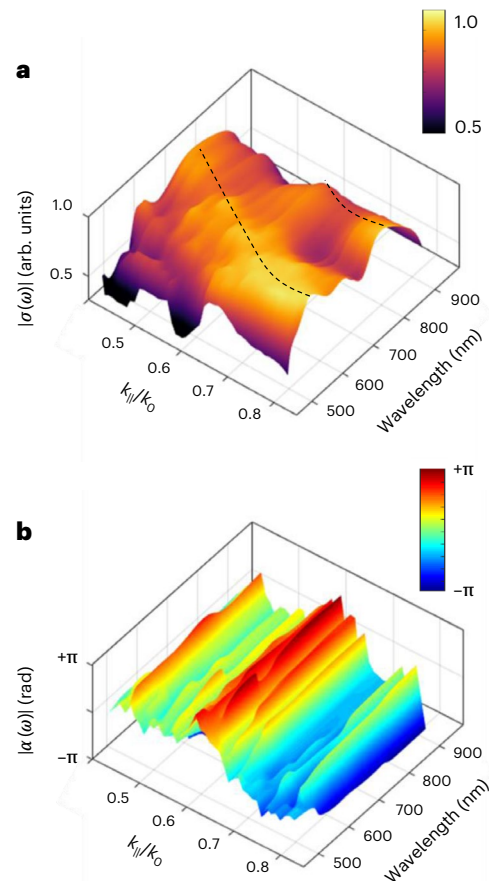

Fig. 5 | Momentum–wavelength map of the relative amplitude and phase of EDPHS and electron-beam excitations. a,b, Retrieved amplitude (**a**) and phase (**b**).

CL spectrum of only EDPHS radiation is easily obtained at the first stage, the electric-field amplitude of only the sample radiation can be retrieved. However, only the differential CL phase between the sample and EDPHS radiation can be acquired with this technique, since no information about the phase of the EDPHS radiation is at hand. The proposed phase-retrieval algorithm should not depend on the delay between the reference and signal, as far as the a.c. and d.c. spectral components are completely distinguishable. This fact can be used as a benchmark for obtaining the accuracy of the proposed technique. Retrieving the intensity and phase at different L values, the fluctuations in the obtained results are negligible for $L = 20$ and $L = 22$ μm. However, the maximum difference of the phase value in the order of 20% is obtained, when comparing the values for $L = 20$ and $L = 30$ μm, which provides an estimate for the accuracy of our spectral interferometry technique.

Thus, the proposed algorithm can be used to retrieve the amplitude ($|\sigma(\omega)|$) and phase ($\alpha(\omega)$) of the momentum–energy maps (Fig. 5). The accuracy of the acquired maps depends on the visibility of the interference fringes, and thus, they are reliable for $0.5k_0 \leq k_\parallel \leq 0.8k_0$. The retrieved amplitude (Fig. 5a) shows a smooth shift in the LP and UP branches towards shorter wavelengths on increasing the transverse momentum (Fig. 5a, dashed lines). This behaviour is expected from the dispersion of exciton–polaritons (strong exciton–photon interactions) for both LP and UP branches. In contrast, the retrieved phase shows fluctuating behaviour versus transverse momentum and a less obvious fluctuation versus wavelength. Considering the lowest-order scattered rays (Supplementary Note 4), the relative phase can

be described as $\alpha_{n=0}(\omega) = k_\parallel l_1 - \beta(\omega) l_1 - \varphi_{T_2}(\omega)$, which is a smooth function of $k_\parallel$. Thus, we notice that the fast fluctuation behaviour of the relative phase is due to the inclusion of higher-order scattering terms.

The correlative photon–electron spectroscopy based on EDPHS, thus, allows for phase-stable spectral interferometry by improving the mutual coherence between the arriving photons and electrons at the sample. The present results, thus, demonstrate a high level of mutual coherence between the sample and EDPHS radiation. Further considerations for improving the technique include the design and realization of EDPHS structures that radiate at an inclined angle, such that the EDPHS radiation does not directly interact with the sample, thereby only providing a reference beam for spectral interferometry. In addition, to retrieve the phase of the EDPHS radiation itself, interfering the EDPHS radiation with transition radiation of a known phase distribution could be considered. Moreover, the compactness of the design allows to minimize decoherence in the photon–electron interaction because the photon generation process happens at a distance of only a few micrometres above the sample. The scheme, thus, maximizes the mutual coherence between the electrons and photons. Intriguingly, advanced nanofabrication techniques could be used to design EDPHS structures with tailored photon emission properties. Generating vortex light or even temporally shaped optical pulses is possible by the control of multiscattering events and engineering defect centres in both lateral and longitudinal directions. The approach, thus, opens new directions in understanding the momentum–spectral correlations in polaritonic materials and correlated electron systems such as transition metal dichalcogenides. Merging this method with advanced holographic techniques[42] allows the unravelling of a variety of information about the charge and energy transfer dynamics ultimately at the attosecond-time resolution. Moreover, this setup has the potential for exploring fundamental aspects of photon–electron interactions and addressing key questions such as entanglement between the generated photons from different scattering events, which could be addressed by combining this with an electron-beam analyser and spectrometer[43] in an SEM[16].

Online content

Any methods, additional references, Nature Portfolio reporting summaries, source data, extended data, supplementary information, acknowledgements, peer review information; details of author contributions and competing interests; and statements of data and code availability are available at https://doi.org/10.1038/s41567-023-01954-3.

References

1. Zewail, A. H. Four-dimensional electron microscopy. *Science* **328**, 187–193 (2010).
2. Feist, A. et al. Ultrafast transmission electron microscopy using a laser-driven field emitter: femtosecond resolution with a high coherence electron beam. *Ultramicroscopy* **176**, 63–73 (2017).
3. Möller, M., Gaida, J. H., Schäfer, S. & Ropers, C. Few-nm tracking of current-driven magnetic vortex orbits using ultrafast Lorentz microscopy. *Commun. Phys.* **3**, 36 (2020).
4. Park, S. T., Flannigan, D. J. & Zewail, A. H. Irreversible chemical reactions visualized in space and time with 4D electron microscopy. *J. Am. Chem. Soc.* **133**, 1730–1733 (2011).
5. Lummen, T. T. A. et al. Imaging and controlling plasmonic interference fields at buried interfaces. *Nat. Commun.* **7**, 13156 (2016).
6. Kurman, Y. et al. Spatiotemporal imaging of 2D polariton wave packet dynamics using free electrons. *Science* **372**, 1181–1186 (2021).
7. Barwick, B., Flannigan, D. J. & Zewail, A. H. Photon-induced near-field electron microscopy. *Nature* **462**, 902–906 (2009).
8. Feist, A. et al. Quantum coherent optical phase modulation in an ultrafast transmission electron microscope. *Nature* **521**, 200–203 (2015).
9. Kfir, O., Giulio, V. D., Abajo, F. J. G. D. & Ropers, C. Optical coherence transfer mediated by free electrons. *Sci. Adv.* **7**, eabf6380 (2021).
10. Dahan, R. et al. Imprinting the quantum statistics of photons on free electrons. *Science* **373**, eabj7128 (2021).
11. Vanacore, G. M. et al. Attosecond coherent control of free-electron wave functions using semi-infinite light fields. *Nat. Commun.* **9**, 2694 (2018).
12. Wong, L. J. et al. Control of quantum electrodynamical processes by shaping electron wavepackets. *Nat. Commun.* **12**, 1700 (2021).
13. Ryabov, A. & Baum, P. Electron microscopy of electromagnetic waveforms. *Science* **353**, 374–377 (2016).
14. García de Abajo, F. J. & Di Giulio, V. Optical excitations with electron beams: challenges and opportunities. *ACS Photonics* **8**, 945–974 (2021).
15. Morimoto, Y. & Baum, P. Diffraction and microscopy with attosecond electron pulse trains. *Nat. Phys.* **14**, 252–256 (2018).
16. Shiloh, R., Chlouba, T. & Hommelhoff, P. Quantum-coherent light-electron interaction in a scanning electron microscope. *Phys. Rev. Lett.* **128**, 235301 (2022).
17. Kfir, O. et al. Controlling free electrons with optical whispering-gallery modes. *Nature* **582**, 46–49 (2020).
18. Talebi, N. Strong interaction of slow electrons with near-field light visited from first principles. *Phys. Rev. Lett.* **125**, 080401 (2020).
19. Dahan, R. et al. Resonant phase-matching between a light wave and a free-electron wavefunction. *Nat. Phys.* **16**, 1123–1131 (2020).
20. Henke, J.-W. et al. Integrated photonics enables continuous-beam electron phase modulation. *Nature* **600**, 653–658 (2021).
21. García de Abajo, F. J., Asenjo-Garcia, A. & Kociak, M. Multiphoton absorption and emission by interaction of swift electrons with evanescent light fields. *Nano Lett.* **10**, 1859–1863 (2010).
22. Park, S. T., Lin, M. & Zewail, A. H. Photon-induced near-field electron microscopy (PINEM): theoretical and experimental. *New J. Phys.* **12**, 123028 (2010).
23. García de Abajo, F. J., Dias, E. J. C. & Di Giulio, V. Complete excitation of discrete quantum systems by single free electrons. *Phys. Rev. Lett.* **129**, 093401 (2022).
24. Yankovich, A. B. et al. Visualizing spatial variations of plasmon–exciton polaritons at the nanoscale using electron microscopy. *Nano Lett.* **19**, 8171–8181 (2019).
25. Arqué López, E., Di Giulio, V. & García de Abajo, F. J. Atomic Floquet physics revealed by free electrons. *Phys. Rev. Research* **4**, 013241 (2022).
26. Li, G., Clarke, B. P., So, J.-K., MacDonald, K. F. & Zheludev, N. I. Holographic free-electron light source. *Nat. Commun.* **7**, 13705 (2016).
27. Adamo, G. et al. Light well: a tunable free-electron light source on a chip. *Phys. Rev. Lett.* **103**, 113901 (2009).
28. van Nielen, N. et al. Electrons generate self-complementary broadband vortex light beams using chiral photon sieves. *Nano Lett.* **20**, 5975–5981 (2020).
29. Talebi, N. et al. Merging transformation optics with electron-driven photon sources. *Nat. Commun.* **10**, 599 (2019).
30. Christopher, J. et al. Electron-driven photon sources for correlative electron-photon spectroscopy with electron microscopes. *Nanophotonics* **9**, 4381–4406 (2020).
31. Wang, Q. et al. Direct observation of strong light-exciton coupling in thin WS_2 flakes. *Opt. Express* **24**, 7151–7157 (2016).
32. Munkhbat, B. et al. Self-hybridized exciton-polaritons in multilayers of transition metal dichalcogenides for efficient light absorption. *ACS Photonics* **6**, 139–147 (2019).

33. Hu, F. et al. Imaging exciton–polariton transport in MoSe$_2$ waveguides. *Nat. Photon.* **11**, 356–360 (2017).
34. Mrejen, M., Yadgarov, L., Levanon, A. & Suchowski, H. Transient exciton-polariton dynamics in WSe$_2$ by ultrafast near-field imaging. *Sci. Adv.* **5**, eaat9618 (2019).
35. Taleb, M., Davoodi, F., Diekmann, F. K., Rossnagel, K. & Talebi, N. Charting the exciton–polariton landscape of WSe$_2$ thin flakes by cathodoluminescence spectroscopy. *Adv. Photonics Res.* **3**, 2100124 (2022).
36. Vu, D. T., Matthaiakakis, N., Saito, H. & Sannomiya, T. Exciton-dielectric mode coupling in MoS$_2$ nanoflakes visualized by cathodoluminescence. *Nanophotonics* **11**, 2129–2137 (2022).
37. Davoodi, F. et al. Tailoring the band structure of plexcitonic crystals by strong coupling. *ACS Photonics* **9**, 2473–2482 (2022).
38. Talebi, N. Spectral interferometry with electron microscopes. *Sci. Rep.* **6**, 33874 (2016).
39. Walmsley, I. A. & Dorrer, C. Characterization of ultrashort electromagnetic pulses. *Adv. Opt. Photon.* **1**, 308–437 (2009).
40. Brenny, B. J. M., Coenen, T. & Polman, A. Quantifying coherent and incoherent cathodoluminescence in semiconductors and metals. *J. Appl. Phys.* **115**, 244307 (2014).
41. Esmann, M. et al. Plasmonic nanofocusing spectral interferometry. *Nanophotonics* **9**, 491–508 (2020).
42. Wolf, D. et al. Unveiling the three-dimensional magnetic texture of skyrmion tubes. *Nat. Nanotechnol.* **17**, 250–255 (2021).
43. Feist, A. et al. Cavity-mediated electron-photon pairs. *Science* **377**, 777–780 (2022).

Methods

CL spectroscopy

Experimental data were collected using a high-resolution SEM using a field emission microscope (Zeiss SIGMA) equipped with a CL detector (Delmic). Here the SEM images are obtained using the secondary electron detector in our SEM setup. We used an acceleration voltage of 30 kV and a beam current of 1–14 nA (based on the experiment) to excite both EDPHS and specimen throughout the measurements. Despite using a high current, we did not observe notable radiation damage. An off-axis aluminium-coated parabolic mirror with a hole for the electron beam (diameter, 600 μm) was directly installed below the pole piece (and below the sample) to collect the generated CL radiation. A nanopositioner stage was installed inside the chamber, and a nanorobotic arm was used to accurately position the EDPHS above the sample stage. The acceptance angle of CL radiation was 1.49 sr and the dwell time of the spectroscopic measurements differs from 50 to 400 ms in different experiments, to account for the long experimental time and signal-to-noise ratio. The collected CL radiation was directed to a charge-coupled device camera for further analysis. Angle-resolved maps were obtained by exposing the sample to electron-beam irradiation with a spot size of 50 nm for 10 s at each step, whereas the energy–momentum CL measurements were acquired by a single exposure (integration time, approximately 150 s) to the electron beam. For mapping the energy–momentum maps, CL radiation was directed through a one-dimensional slit opening, where a diffraction grating dispersed it on a two-dimensional charge-coupled device array, with the momentum components defined by the slit mapped in the vertical direction, yielding a map of $I(k, \lambda)$. The obtained bare charge-coupled device image was mapped onto the energy–momentum space, considering the parabolic shape of the mirror, magnification of the optical path and camera pixel size.

Numerical simulations

To numerically explore the mutual coherence and interference effects, we performed several simulations using the finite-difference time-domain method. In particular, we used this technique to simulate the spatiotemporal distribution of EDPHS radiation. The obtained EDPHS radiation was then superimposed with the electron-beam excitations to excite the sample in a sequential way by altering the delay between the electron and EDPHS radiation. To perform the simulations, the home-built numerical code described elsewhere and the supercomputing cluster at Kiel University have been used. Full details about the parameters and simulation times are presented in Supplementary Notes 1 and 4.

Data availability

Source data are available for this paper. All other data that support the plots within this paper and other findings of this study are available from the corresponding author upon reasonable request.

Code availability

The numerical code used to simulate the data is available from the corresponding author on reasonable request.

Author contributions

M.T. performed the experiments, designed and realized the nanopositioner stage, and analysed the data together with N.T. M.H. fabricated the EDPHS structure. K.R. produced the WSe$_2$ crystals in his group. N.T. conceived the data, designed the experimental configuration and performed the simulations. N.T. wrote the manuscript with contributions from all the co-authors.

Competing interests

The authors declare no competing interests.

Additional information

Supplementary information The online version contains supplementary material available at https://doi.org/10.1038/s41567-023-01954-3.

Correspondence and requests for materials should be addressed to Nahid Talebi.

Peer review information *Nature Physics* thanks the anonymous reviewers for their contribution to the peer review of this work

Reprints and permissions information is available at www.nature.com/reprints.